

Rich Methane Oxidation on Pt/Pd/Al₂O₃: Steady State Performance, Multiplicity Features, and Spatial Patterns

Jonathan Ratcliff, Kyle Karinshak, and Michael P. Harold*

William A. Brookshire Department of Chemical and Biomolecular Engineering, University of Houston, Houston, Texas 77204, USA

*Corresponding author: mpharold@central.uh.edu

Abstract

Novel features are reported for the catalytic sub-stoichiometric (rich) oxidation of methane on a Pt+Pd/Al₂O₃ washcoated monolith over a range of feed temperatures (450 – 575 °C) and O₂/CH₄ concentration ratios (0 to 2) for both dry and wet (2.5% H₂O) feeds. Near isothermal steady state multiplicity and co-existing states with vastly different methane conversions are presented. Systematic variation in the O₂ feed concentration reveals a higher conversion, active regime at lower O₂ feed concentrations characterized by positive-order dependence on O₂ and weak temperature dependence, and a lower conversion, inhibited regime at higher O₂ feed concentration characterized by a negative-order O₂ dependence. The methane conversion maximum is accompanied by an overlap of the two regimes in the form of a clockwise hysteresis loop; i.e., steady-state multiplicity. Spatial measurements of reacting species concentration profiles for the dry feed reveal an upstream oxidation zone and downstream CH₄ steam reforming zone. Spatial measurements extending beyond the catalyst reveal the co-existence of active and inhibited states within the multiplicity region. Addition of excess water increases the methane conversion and promotes concurrent methane oxidation and steam reforming. The multiplicity and nonuniform states persist with the wet feed. Underlying mechanistic aspects responsible for the inhibition, rate multiplicity and co-existing states are proposed and discussed.

Keywords: Methane; Oxidation; Reforming; Platinum; Kinetics; Multiplicity;

1: Introduction

There is renewed interest in natural gas vehicles (NGVs) and engines (NGEs) given that methane (CH_4), the major component of NG, has a more ecologically favorable H:C ratio compared to petroleum-based fuels. However, CH_4 that is not consumed during internal combustion is likely to escape conventional emission control catalysts. This “methane slip” must be eliminated since CH_4 itself is a ~ 25 x more potent greenhouse gas (GHG) than CO_2 . To this end, advances in methane oxidation catalysts (MOCs) are needed that are much more effective in abating methane and in meeting more stringent emissions regulations. Such advances are especially critical in engine applications in which electrification will have a slower adoption.

Platinum group metals (PGM) such as Pt and Pd are the most active metals for catalytic oxidation of methane and are therefore likely to be included in next generation MOC formulations. Pre-2000 reviews of the catalytic oxidation of methane have appeared [1,2]. Oh and Mitchell [3] showed ~ 30 years ago that the methane conversion achieves a maximum value as $\lambda \rightarrow 1$, where λ (“lambda”) is the dimensionless O_2/CH_4 molar ratio. For O_2/CH_4 to the left of the maximum the Pt surface has sites available for CH_4 adsorption. Earlier studies, along with more recent studies highlighted by Bugosh et al. [4], established Pt as the most active metal for methane conversion when the oxidation is to the rich of stoichiometric. As $\text{O}_2/\text{CH}_4 \rightarrow 2$ ($\lambda \rightarrow 1$) the oxygen coverage increases. To the right of the maximum the rate (conversion) decreases due to oxygen inhibition. Chin and Iglesia [5] showed that CH_4 activation is most effective on a site pair comprising Pt-O and Pt.

On the other hand, PdO is known to be the most active PGM for abating methane in the lean combustion regime ($\text{O}_2/\text{CH}_4 > 2$, $\lambda > 1$) [2], although the identity of the active site remains under debate [6]. PtO is a comparatively inactive catalyst for lean methane oxidation [5]. A catalyst

containing both Pt and Pd can result in performance exceeding that of either Pt or Pd alone over a range of conditions [7-9].

A subset of surface catalyzed reactions is known to exhibit multiple rate states, sometimes referred to as rate multiplicity. Most reports of multiplicity have been of noble metal (Pt, Pd) catalyzed CO oxidation [10-17]. The underlying origin of multiplicity is a nonlinear coupling of the surface kinetics alone or nonmonotonic single-valued kinetics coupled with mass and/or heat transport processes. Thermokinetic multiplicity, arguably the most common type, arises from coupling between linear external mass and heat transport processes and nonlinear reaction heat generation. Hysteresis can also be observed during temperature ramping experiments that is a spatio-temporal outcome of the experimental method [18]. This arises from the heat released via oxidation propagating the reaction even as the feed temperatures have decreased to a point of diminished reaction. Eigenberger [19] introduced the concept of multiplicity originating from the surface rate processes alone. Here concentration-based hysteresis is a result of coupling of adsorption, surface reaction, and desorption steps for which more than one step is rate limiting [19-22]. Isothermal coupling between either external or intraparticle transport and nonmonotonic kinetics may mask underlying intrinsic kinetic multiplicity. Multiplicity observed during methane oxidation is less commonly reported. Amin et al. [23] attributed methane conversion hysteresis to a temperature dependent PdO formation. More recently Bugosh et al. [4] reported isothermal rate multiplicity for rich methane oxidation on Pt+Pd/Al₂O₃ monolith and attributed it to intrinsic kinetic coupling. Thermal effects were ruled out given the rather low methane concentration used (< 1000 ppm).

While methane oxidation is the main reaction of interest, methane steam reforming (SMR) and water-gas shift (WGS) may also occur at elevated temperature. Both SMR and WGS obviously

require H₂O which creates a chemical coupling between complete oxidation (upstream) and SMR+WGS (downstream). Moreover, thermal coupling occurs between the exothermic oxidation and WGS and the endothermic reforming. These coupling effects can be studied in more detail with spatially-resolved measurements of species concentration and temperature. Spatially-resolved concentration measurements are accomplished with capillary inlet mass spectrometry, or SpaciMS [4,24]. This technique involves sampling and analyzing the mass spectra of a small fraction of the flowing reaction mixture within a monolith channel. By moving the capillary probe concentration profiles are constructed. Previous studies have examined the extent of the invasiveness of the capillary within the channel, with some saying it is minimally impactful while others say there is an effect on the measured profiles [25-27]. The spatially resolved temperature is obtained using coherent optical frequency domain reflectometry, or c-OFDR [28,29]. This method uses a laser launched through a fine optical fiber positioned within a monolith channel. The scattering pattern of the reflected is processed to obtain the spatial distribution of temperature along the fiber [30]. Previous work has been done to understand the spatial features of rich CH₄ oxidation, techniques on monometallic catalysts [31,32]. These studies also used either translatable devices to measure temperature discretely along the length of the catalyst [32] or used non-in situ measurements [33].

The present study is focused on the steady state features of the methane rich oxidation on a Pt rich (Pt:Pd = 19:1, mass basis) monolith catalyst over a range of feed temperatures and composition. Spatially-resolved measurements within a monolith channel of the concentration and temperature supplement conventional effluent measurements of integral conversion and selectivity. Special attention is placed on identifying multiplicity features and nonuniform states. The addition of H₂O provides a detailed assessment of competing oxidation and reforming

pathways. Underlying mechanistic aspects responsible for the inhibition, multiplicity and nonuniform states are proposed and discussed.

2: Experimental

Experiments were carried out on a 600 cpsi (cells per square inch) monolith catalyst provided by CDTi (Oxnard, CA). The catalyst contains two precious metals, Pt and Pd (PGM for short), with a total PGM loading of 30 g PGM/ft³ monolith and a Pt:Pd ratio (mass) of 19:1. The metals are supported by a γ -Al₂O₃ washcoat with a loading of 100 g/L monolith. The monolith dimensions are 2.54 cm (diameter) by 1 cm (length).

The monolith was wrapped in FiberfraxTM ceramic paper (to prevent bypassing) and contained within a 2.7 cm ID quartz tube, which itself is located within a large clamshell furnace (Lindberg/Blue M). To minimize axial temperature gradients, a ceramic ring heater was positioned upstream of the monolith on the outside of the quartz tube [24]. This design serves to preheat the feed gas mixture and flattens the temperature profile within the furnace. In a typical experiment the furnace temperature was set ~50 °C below the desired feed temperature while the ring heater was primarily responsible for achieving the desired feed temperature.

Optical frequency domain reflectometry (OFDR) was employed to measure the spatial temperature profile. An optical fiber probe (125 μ m o.d.) is inserted into one of the monolith channels located near the cross-sectional center. The probe is connected to the reflectometer (Luna Technologies, Blacksburg, VA; model OBR 4600). The optical fiber wall consists of two layers, an inner silica shell through which a laser pulse is directed, and an outer gold coating to render the fiber inert. The pulse that is reflected back to the device comprises a scattering pattern that is

converted into a spatial temperature using a calibration between spectral shift and temperature [28]. Details are provided by Peng et al. and Nguyen et al. [26,28]. In the current study, an uncoated (blank), 600 cpsi cordierite monolith of length 2.5 cm was positioned 20 mm downstream of the active monolith. This piece provides additional support for the fiber and helps to reduce vibrations from flow which increases signal noise. The active monolith was rotated around its axis so that the fiber rests in a corner of the square channel. This location minimizes the potential intrusive impact of the fiber on the flow, and hence reaction, within the channel [25]. For the conditions employed a spatial resolution of 3 mm was achieved [28,29]. For all of the experiments, the reference temperature was ambient (~ 22 °C).

Species concentration profiles are obtained using an in-house constructed capillary inlet spatially-resolved mass spectrometer (SpaciMS). Details of the SpaciMS system are provided by Nguyen et al. [24]. The flowing gas mixture was sampled by a 170 μm o.d. quartz SpaciMS capillary and directed to a Balzers (Prisma) mass spectrometer. The capillary was contained in a quartz tube (3.3 cm o.d.) while its position was translated during the reaction experiments. The capillary tip was positioned either within a monolith channel or downstream of the monolith (up to 1 cm beyond back face) to collect reactor and post-reactor species concentration data, respectively. Three-point calibrations were performed for the reacting species of interest (CH_4 , CO , CO_2 , O_2) using the Ar diluent as an internal standard. Gas flows were controlled by MKS mass flow controllers with the gases all being ultra-high purity supplied by Matheson Tri-Gas.

3: Results and Discussion

Rich Methane Oxidation Trends for Dry Conditions

A parametric evaluation was conducted of sub-stoichiometric (rich) methane oxidation to evaluate the impacts of feed composition and temperature. The feed concentration of oxygen spanned a range of $O_2:CH_4 = 1:15$ to $2:1$ while the CH_4 feed concentration was fixed at 4200 ppm. Unless otherwise specified, all experiments had a total flowrate of 8 L/min (@ STP) corresponding to a gas hourly space velocity (GHSV) of $100k\text{ hr}^{-1}$ based on the monolith volume. For each composition the feed temperature varied from 450 to 575 °C.

Appreciable variation in the methane conversion and product distribution were encountered during the parametric study. Figure 1 shows the dependence of the CH_4 fractional conversion (Fig. 1a), and the effluent concentrations of CO_2 (Fig. 1b) and CO (Fig. 1c) as functions of the feed O_2 concentration and feed temperature. The shape of the CH_4 conversion plots is the same for each of the temperatures considered and consists of three regimes. (We discuss later a fourth regime, which is not evident in Fig. 1.) At lower O_2 concentration there is a nominally linear, positive order regime while at higher O_2 concentration the conversion has a negative order dependence on O_2 . For each feed temperature there is an intermediate O_2 feed concentration at which the conversion reaches a maximum. We refer to the positive-order regime as *the active regime* and the latter as the *inhibited regime*. The *inhibited regime* is divided into two parts, i.e., *partial inhibited regime* and *full inhibited regime*. The distinction between the two sub-regimes concerns the sensitivity of the methane conversion to the O_2 concentration. In the *full inhibited regime*, the conversion is largely independent of the O_2 concentration. As an example, at 525 °C, the *active regime* spans 0 to 3000 ppm O_2 , the *partial inhibited regime* spans 3000 to 5200 ppm O_2 , and the *full inhibited regime* spans 5250-9000 ppm O_2 .

Each regime have distinct dependencies of the methane conversion on temperature. The O_2 feed concentration at which the CH_4 conversion is maximum is an increasing function of feed

temperature. In the active regime, for sufficiently low O₂ concentrations (approach zero) the temperature dependence is very weak, indicating a strongly O₂ feed limited state. For O₂ concentrations somewhat less than the concentration giving the maximum conversion the temperature dependence is nonmonotonic. For example, between 1800 ppm and 3000 ppm O₂ the CH₄ conversion is higher at 525 °C than at both 550 °C and 575 °C. The origin of this phenomenon will be described later. To the right of the maximum the methane conversion is a moderately increasing function of temperature, somewhat more sensitive in the *partial inhibited regime* compared to *full inhibited regime*.

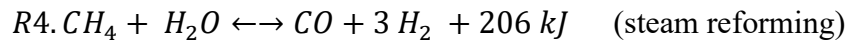
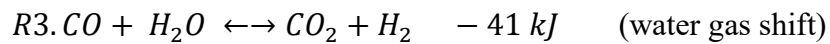
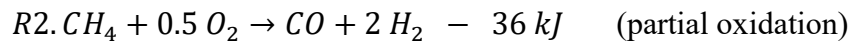
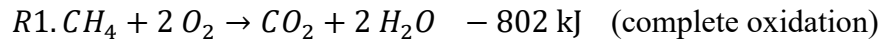
The CO₂ effluent concentration dependence on O₂ feed concentration shown in Fig. 1b generally mirrors the methane conversion trends. At lower O₂ feed concentration the CO₂ concentration is nearly linear between the origin and conversion maximum. The conversion dependence on feed temperature shows the same negative order behavior described above. Beyond the maximum, the CO₂ concentration sharply drops to a low but nonzero level.

In contrast to the CH₄ conversion and CO₂ concentration plots, the CO effluent concentration vs. O₂ feed concentration in Fig. 1c has a distinct convex shape to the left of the maximum. The negative temperature trend for the conversion and effluent CO₂ is clearly evident in the CO concentration plots. For example, for a fixed O₂ feed concentration of 3000 ppm the effluent CO concentration is ~800 ppm at 525 °C but only ~425 ppm at 575 °C. Finally, the CO concentration is essentially zero in the *partial* and *full inhibited regimes*.

Spatially-resolved concentration profiles were obtained at an O₂ feed concentration of 2700 ppm and feed temperature of 525 °C. Fig. 2a (2b) show the profiles for CH₄ and O₂ (CO₂, CO, and H₂O). Near the inlet of the monolith, measurable but negligible methane oxidation occurs. The existence and length of this oxidation zone depends on the O₂ feed concentration. At

2700 ppm O₂ the zone has a length of ~4mm. The length of this zone scales directly with the feed O₂ concentration, with lower concentrations decreasing and higher concentrations increasing the length. Eventually this region is long enough to span the entire monolith channel resulting in an inhibited channel with reduced methane conversion. Clearly, this trend underscores the existence of O₂ inhibition.

It is instructive to analyze the features in the data in Figs. 1 and 2 (described next) in the context of the overall reactions that are thought to be occurring:



As described above for the experiment with a feed temperature of 525 °C and O₂ feed concentration of 2700 ppm, the CH₄ concentration decreases slowly from the front face, then more sharply over a narrower zone. Between 4 and 6 mm ~1000 ppm of methane is consumed. Within the 2 mm zone nearly complete conversion of O₂ is achieved. The rapid consumption of O₂ points to the predominance of oxidation chemistry; specifically, complete CH₄ oxidation to CO₂ (reaction R1) and partial CH₄ oxidation to CO (R2). The sharp increase in the CO₂ concentration within this region (Fig. 2b) shows that complete oxidation drives the CH₄ conversion. It is noted that a negligible but non-zero concentration of O₂ is present at the 6 mm mark. The modest increase in CO between 6 and 8 mm but nearly constant level of CO₂ suggests the occurrence of CH₄ partial oxidation (R2). That said, the ~300 ppm increase in CO is not solely attributable to partial oxidation. We will expand on this point next.

Once the O₂ is depleted the primary chemistry shifts from aerobic to anaerobic reactions, the latter including methane steam reforming (SMR; reaction R4) and water-gas shift (WGS; reaction R3). SMR is likely responsible for the continued conversion of CH₄ in the final 3-4 mm of the reactor. It is noted that since the reactor feed is “dry”, the H₂O required for SMR and WGS is provided by the upstream total oxidation. This fact plays a pivotal role in the resulting effluent CO and CO₂ concentrations. The influence of WGS and SMR is also seen in the calculated H₂O profiles (calculation explained in Supplementary Material, section S.3). The concentration of H₂O exhibits a maximum at the end of the oxidation zone prior to reforming reactions (SMR and WGS). This further reinforces the sequential nature of oxidation and reforming reactions.

Complete oxidation not only generates H₂O but also heat. The upstream oxidation is highly exothermic ($\Delta H_o = -802$ kJ/mole), resulting in heat that is carried downstream by the flowing gas and the conducting monolith to the anaerobic section where SMR occurs ($\Delta H_o = 206$ kJ/mole). It is noted, however, that the exothermic reaction heat is only a supplement of the heat supplied by the furnace since the reactor is nonadiabatic. The OFDR measured temperature profile provides evidence for the thermal coupling. Fig. 2c compares the temperature profile during reaction to that obtained during flow (at the same rate) of inert Ar only. The temperature increase due to reaction is up to ~30 °C higher at the 10 mm mark. In addition, a slight temperature decrease in comparison to the inert is encountered due to the endothermic reforming reaction. The measured temperature rise in the oxidation zone may be compared to the expected rise under adiabatic conditions. Knowing the CO/CO₂ (0.34) and CH₄ conversion (0.509) at the 10 mm mark, the estimated temperature rise is 46 °C. The SM contains the details of the estimation. The lower value obtained experimentally is attributed to heat loss.

With insight provided by the measured concentration profiles, we can analyze other pertinent features in the CH₄ conversion, CO₂ and CO effluent concentration versus O₂ feed concentration data in Fig. 1. The explanation of those features is provided in the Supplementary Material.

The generation of carbon during sub-stoichiometric methane oxidation is possible. A carbon balance for the different feed conditions (O₂ concentration and temperature) was carried out. The carbon was balanced within +/- 7% below 575 °C of the carbon fed. The 575 °C experiment revealed the formation of carbon at lower O₂ concentration followed by consumption at higher concentrations (Fig. S.3). This is expanded upon in the SM.

Kinetic and Steady State Multiplicity Features for Dry and Rich Methane Oxidation

A fourth prominent feature in the methane conversion data emerged from the parametric study. The experiments shown in Fig. 1 were obtained through a gradual increase in the O₂ feed concentration starting from O₂ concentration near 0 ppm to the stoichiometric level (8400 ppm for the 4200 ppm CH₄ feed). Prompted by earlier findings of Bugosh et al. [4], the O₂ variation direction was reversed to check for possible hysteresis. The results for feed temperatures of 500, 525, and 550 °C are shown in Figure 3. We will focus on the 525 °C data but the points of interest apply to the other temperatures. Starting with an O₂ feed concentration of 6000 ppm and a methane conversion on the order of 5%, the conversion remains below 10% as the O₂ feed concentration slowly decreases. Upon reaching 2100 ppm the conversion increases abruptly and settles along the upper active branch described earlier. Thus, the inhibited branch extends well into the range of O₂ concentrations for which the active state was observed. The clockwise hysteresis in the CH₄ conversion as a function of O₂ feed concentration corroborates the earlier findings of Bugosh et

al. [4] who reported hysteresis at a somewhat lower CH₄ concentration of 800 ppm for an equimolar Pt+Pd/Al₂O₃ washcoated monolith. A distinguishing feature in these new findings is the rather unconventional shape of the upper branch between the maximum and the lower conversion branch. Most previous reports of conversion/rate multiplicity comprise distinct ignition and extinction (bifurcation) points. The data in Fig. 3 reveal a more gradual decrease in the upper branch down to the vicinity of the lower branch. Below we describe the root cause for this interesting feature.

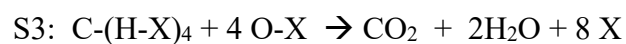
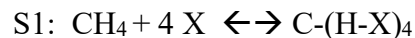
As mentioned in the last paragraph, we also found hysteresis at other feed temperatures (500, 550 °C in Fig. 3, and 575 °C), in line with the Bugosh et al. [4] study that used a lower CH₄ feed concentration of 1500 ppm. For each of these, an inhibited branch extends into the previously measured active branch as the O₂ concentration decreases. The main difference in the hysteresis loops for the different feed temperatures is their size and location. With increasing temperature, the multiplicity region moves to higher oxygen concentrations. The 500 °C hysteresis is the smallest, consistent with the active branch moving to a smaller range of O₂ concentrations. Later in the paper we present conversion hysteresis data for a feed containing water.

A number of mechanistic and kinetic studies of the catalytic oxidation of methane on Pt and Pd have appeared. The reaction sequence is known to involve the conventional steps of CH₄ and O₂ adsorption and surface reaction. A large number of adspecies are present, such as CH_x (x = 0 to 4), H, and O. Reaction between oxygen adatoms and CH_x (x = 0 to 4) leads to products CO, CO₂, H₂, and H₂O. Rate inhibition by O₂ is a well-established feature of Pt and Pd catalyzed methane oxidation. Site blocking by adsorbed oxygen occurs due to the strong binding that occurs between O and Pt. At sufficiently high gas phase O₂ concentration (or partial pressure), the adsorbed oxygen coverage inhibits methane adsorption and reaction. As the concentration of

oxygen decreases, the observed small increase in conversion suggests that oxygen coverage gradually decreases but remains high enough to suppress reaction. As the data show, oxidation is initiated discontinuously from the inhibited to active state. The existence of a maximum conversion (rate) at an intermediate O_2 is a necessary but not sufficient feature for the clockwise hysteresis. Kinetic models have been proposed for methane oxidation that predict the maximum but not the hysteresis. For example, Chin and Iglesia [5] propose the existence of three kinetic regimes defined by the CH_4/O_2 ratio during methane oxidation on Pt. They propose an apparent order of -1 with respect to O_2 partial pressure in the inhibited regime.

The existence of multiplicity and the clockwise hysteresis pattern suggests a kinetic origin with possible contribution of mass transport. Isothermal rate multiplicity has been reported by a number of experimental studies, with Pt-catalyzed CO oxidation being the most common reaction system [11-17]. The pioneering studies of Eigenberger [19] shows that the coupling between adsorption, desorption and surface reaction may cause a multi-valued rate or rate multiplicity. Criteria for site blocking are derived for selected bimolecular sequences. A main finding is that the number of sites required for adsorption of the non-inhibiting reactant must exceed the number of sites required for adsorption of the inhibiting reactant.

Applying the Eigenberger multiplicity analysis to methane oxidation, the non-inhibiting reactant is CH_4 and the inhibiting reactant is O_2 . Consider the following simplified mechanistic sequence for the complete oxidation of CH_4 :



It is noted that the number of sites for inhibiting O₂ to adsorb is 2 while the number of sites for non-inhibiting CH₄ to adsorb is 4. The sequence contains the essential adsorption and desorption steps involving CH₄ and O₂. The dissociative adsorption of O₂ on Pt and Pd is well established. The adsorption of CH₄ has been shown to occur through a series of dehydrogenation steps. Assuming mass action kinetics and no single rate limiting step, the resulting model is a multi-valued function of the O₂ concentration. On the other hand, if the surface reaction step S3 is assumed rate limiting and the adsorption steps are equilibrated, a single-valued rate expression results that predicts the existence of a maximum in the rate for an intermediate O₂ concentration.

Spatially Nonuniform States

Further examination of monolith reactor performance within the region of conversion multiplicity reveals a coexistence of both inhibited and active states. To our knowledge, this phenomenon has not been reported previously for a monolith reactor. The nearly nonexistent mass coupling and limited thermal coupling between parallel monolith channels allows for some channels to be inhibited while others remain active. The data is conclusive. Figs. 4a and 4b show two pairs of SpaciMS-measured CH₄ and O₂ concentration profiles obtained under the same operating conditions but in separate (successive) experiments. The probe intentionally spans the entire length of the monolith (0 – 10 mm) and beyond the back face (10 – 20 mm). In one channel a high methane conversion (active) is sustained while in another a low methane conversion (inhibited) is sustained. The measured channels are located within a small region of the catalyst cross-section (i.e., adjacent channels). In fact, it cannot be said for certain whether the data are from the same channel (or not). The active channel has a profile shown previously for active channel species profiles. There is an upstream zone ($z < 6$ mm) with negligible CH₄ conversion

followed by a zone ($6 < z < 10$ mm) with much higher conversion. Beyond the back face ($z > 10$ mm) the conversion reaches a maximum ($\sim 50\%$) and then declines to $\sim 30\%$. Specifically, the conversion at the 12 mm mark (2 mm behind the back face) shows little difference from the conversion at the back face. As distances further downstream the methane conversion decreases, approaching a level comparable to the level from the inhibited channel experiment. Notably, the corresponding O_2 profile in Fig. 4b shows that O_2 consumption occurs at the 6 mm mark within the monolith but O_2 reemerges beyond the back face. Thus, despite almost complete conversion of O_2 in the active channel, there is apparent breakthrough of unreacted O_2 . Interestingly, the measured CH_4 conversion at the 20 mm mark is consistent with the value measured in the earlier experiments (Fig 1).

The presence of separate inhibited channels was detected during another experiment carried out under the same operating conditions. For an inhibited channel, the rate of methane conversion is relatively constant throughout the entire length. The O_2 concentration remains close to its feed value. As the capillary is removed from the monolith, a rather abrupt increase in methane conversion is encountered despite the post monolith region containing no catalyst. The methane conversion increases to the same level as the active channel. Importantly, the existence of inhibited channels rules out any possible intrusion by the capillary in leading to these results.

These collective features suggest that some channels may not be active and that the “mixed output” represents an average of active and inhibited channels. Flowing gas leaving these channels mix beyond the back face of the monolith. The active channel shows complete consumption of O_2 well before the end of the catalyst but the reemergence of O_2 downstream of the back face. The post monolith increase in O_2 rules out any possible chemical reaction, i.e., formation of O_2 would require the reverse of oxidation which is unlikely since methane oxidation is strongly irreversible.

The potential for bypassing was ruled out by performing “slip check” experiments. This involved carrying out CO oxidation which should achieve complete conversion under these conditions. Complete CO conversion was achieved. It should be mentioned that bypassing around the periphery of the monolith would only explain the trends observed for the active channel but not for the inhibited channel.

The presence of active channels with complete O₂ conversion followed by a reduction in conversion in the post-catalyst region was also detected at 3300 and 3600 ppm O₂ feed concentration and feed temperature of 525 °C. This implies that the partial inhibited region that exists between the point of maximum CH₄ conversion and the inhibited region is attributed to the contribution from active and inhibited channels. As the O₂ feed concentration is increased beyond the conversion maximum, channels become inhibited. This results in a reduction in the overall methane conversion. As the O₂ is further increased from this point, more channels become inhibited until all of the channels are inhibited, and the conversion decreases accordingly. The conversion previously observed during the inhibited region can only be obtained via multiple independent channels averaging to a value and not by any singular channel.

Earlier the rather unusual shape of the active branch to the right of the maximum was noted (Fig. 3). We believe that the origin of the gradual rather than abrupt decrease in conversion from the active branch to the inhibited branch is rooted in the coexisting states. Points are circled in Fig. 3 for which the co-existence of low and high conversions was confirmed. That is, the measured conversion contains contributions from both active and inhibited channels. As O₂ is increased eventually all of the channels become inhibited and there is a merging of the high and low branches.

Effect of Water on Rich Methane Oxidation

The results presented to this point all consist of feeds containing only CH₄, O₂, and Ar. In this section we describe results with H₂O included in the feed. As will be seen, the “dry feed” methane oxidation data are more complex than the “wet feed” data. The results of the parametric evaluation of feed temperature and O₂ feed concentration are in Figs. 5a-c. The feed temperatures span a smaller range than for the dry feed experiments (475 °C to 550 °C), while the O₂ feed concentrations span the same range (0 to 9000 ppm).

Inclusion of water in the feed, not surprisingly, results in an increase in the contribution of methane steam reforming to the overall methane consumption (Fig. 5a). This is clearly evident for the feed devoid of O₂. In that case the dry feed shows negligible methane conversion. It should be mentioned that the temperature range considered rules out methane decomposition/pyrolysis. Muradov and Veziroğlu report that 700-1000 °C is needed for Pt catalyzed CH₄ decomposition [34]. The wet data show that a methane conversion of 20% is attained at the lowest temperature of 475 °C, increasing monotonically with feed temperature. The formation of CO clearly points to steam reforming (R4). In turn, the non-negligible formation of CO₂ suggests the occurrence of water gas shift (R3). Recall that the spatial profiles for the dry feed clearly show that when O₂ is present CO₂ is the main C-containing product, a result of complete oxidation (Fig. 2b). Further, since SMR produces CO, the addition of 2.5% H₂O promoting WGS results in a decrease in the CO/CO₂ ratio.

When O₂ is introduced into the wet feed several distinct regimes appear in the dependencies of methane conversion, and CO and CO₂ effluent concentrations on O₂ feed concentration (Fig. 5b and 6c). The first of these is seen in the lower range of O₂ concentrations bounded below by the anaerobic feed, wherein the methane conversion monotonically increases with O₂ concentration.

This regime is largely similar to the *active regime* in the dry feed case. One difference for the wet feed is the monotonically increasing dependence on temperature (for fixed O_2). The addition of 2.5% H_2O clearly shifts the identity of the limiting reactant for steam reforming from H_2O to CH_4 . As the feed temperature increases, the rate of steam reforming increases which increases both methane conversion and CO production. The CH_4 conversion approaches much higher levels compared to the dry feed, for which the supply of O_2 is limiting and the temperature dependence is weak.

Within the *active regime* for the wet feed the effluent CO_2 concentration dependence on O_2 concentration exhibits a linear increase up to the fall-off at higher concentration (Fig. 5b). Moreover, the dependence on temperature is rather weak. These features are similar to those of the dry feed (Fig. 1b) since O_2 is the limiting reactant for oxidation. The increasing CO_2 formation indicates increasing oxidation and WGS conversion of CO.

In contrast, the CO effluent concentration is comparatively insensitive to O_2 feed concentration but more sensitive to the feed temperature. In particular, the CO dependence on O_2 does not possess the convex shape obtained in the dry feed experiments (Fig. 5c). Rather, the flat CO concentration suggests a balance between its formation by SMR and its consumption by WGS and oxidation. The surplus of H_2O increases both the rate of steam reforming (R4) and water gas shift (R3). Increases in temperature result in an increase in the rate of SMR producing the temperature dependence seen for CO. The much higher CO concentrations at low O_2 compared to the dry feed underscores the increased role of SMR and WGS. Thus, the change in shape is a result of the above-mentioned increased role of SMR and WGS.

At sufficiently high O_2 concentration the conversion reaches a maximum and proceeds to decrease with further increase in the O_2 concentration. This inhibition regime, as in the dry case,

can once again be split into two sub-regimes; the first sub-regime is partial inhibition and the second is full inhibition. The persistence of O₂ inhibition for the wet feed shows that site blocking of methane reforming and oxidation is still possible. Hysteresis in the form of multiple steady states is also encountered for the wet feed. We present the data below.

Comparison of the spatially-resolved concentration profiles for the dry and wet feeds provides additional insight into the competing reactions. Figs. 6a-d show the species profiles at a feed temperature of 525 °C and O₂ feed concentration of 2700 ppm for wet and dry feeds. For this set of conditions all channels are active, and no inhibited states were encountered. A comparison of the CH₄ conversion profiles in Fig. 6a shows the elevated activity (conversion) for the wet feed. The primary region of reaction for the wet feed is between 2 and 4 mm, wherein about 40% of the methane is converted. The corresponding CO₂, CO, and O₂ profiles exhibit the shift to upstream for the wet feed. For otherwise identical conditions except for an absence of H₂O in the feed, the active zone occurs further downstream, i.e., between 4 and 6 mm. These data suggest concurrent oxidation and steam reforming for the wet feed, in contrast to the sequential behavior for the dry feed.

For the dry feed there is a clear demarcation between an oxidative zone and reforming zone (Fig. 6b and 6c). CO does not appear until most of the O₂ is depleted. This is not the case for wet feed. A non-negligible CO concentration is measured at the O₂ depletion point. The co-generation of CO and CO₂ indicates a co-existence of methane steam reforming and oxidation. Addition of excess H₂O boosts reforming.

Examination of the extents of reaction for a network consisting of steam reforming, total oxidation, and water-gas shift shows that this region not only has concurrent steam reforming, but

also water-gas shift. This adds to the amount of CO_2 produced in this region from total oxidation. Further information about the extent of reaction analysis is provided in the SI.

The earlier depletion of O_2 for the wet feed suggests reduced O_2 inhibition. Downstream of the 4 mm mark, oxygen is depleted so the reactions that continue to occur are only steam reforming and water-gas shift. With the O_2 depletion occurring sooner (further upstream), a larger section of the reactor is available for methane steam reforming and water gas shift. Steam reforming is responsible for the continued consumption of methane along with the production of CO . The continued formation of CO_2 post oxygen depletion is solely from water-gas shift.

The catalyst can still be divided into two sections, an oxidative-reforming region, and a reforming region. However, the oxidative-reforming region does not consist solely of oxidative reactions, as is the case for a dry feed. Instead, all reactions are possible, but oxidative reactions are solely located in the oxidative-reforming region. Both steam reforming and water-gas shift continue to be prevalent in the reforming region with steam reforming have a slower rate than was observed within the oxidative region.

It is of interest to know if the addition of water to the feed affects the existence and features of the steady state multiplicity observed for the dry feed. With this in mind, experiments were carried out with 2.5% H_2O in the feed, following the earlier procedure of starting at a high O_2 feed concentration with the catalyst in the inhibited regime and then progressively lowering the concentration by small increments. The results shown in Fig. 7 for a feed temperature of 525 °C and a starting O_2 concentration of 5700 ppm with decreasing increments of 300 ppm reveal the existence of the clockwise hysteresis loop. Starting with a methane conversion of ~5% at 5700 ppm O_2 , the conversion gradually increases with decreasing concentration, reaching ~10% by 2400 ppm O_2 . A further 300 ppm O_2 decrease resulted in an abrupt jump from the inhibited branch to

active branch, eventually settling at ~60%. The O₂ concentration was then gradually increased, following the previously measured active branch.

A potential kinetic mechanism involving site blocking of methane adsorption by oxygen was proposed earlier to explain the existence of the isothermal multiplicity for the dry feed. That the multiplicity persists for a wet feed minimally suggests the additional chemistry involving water does not remove the underlying reason for the hysteresis. That the O₂ feed concentration at the ignition point is the same for both the dry and wet feeds (2100 ppm) suggests that surface oxygen remains the site blocker. This is despite the inhibition point for a given temperature being at a higher O₂ feed concentration under wet conditions than under dry conditions.

Finally, we checked if the nonuniform state behavior observed with the dry feed is encountered with the wet feed. Recall for the dry feed active and inhibited states could co-exist at the same operating conditions resulting in a pseudo-inhibited conversion level (Fig. 4). We ran an experiment with a feed temperature of 525 °C and O₂ feed concentration of 3900 ppm O₂ with 2.5% H₂O in the feed and proceeded to probe the spatial features of multiple channels.

Fig. 8 shows a spatial profile for O₂ under the same feed conditions of 525 °C and 3900 ppm O₂. The profile shows complete consumption of O₂ by the 6 mm point. This is obviously an active channel. At distances further down the length of the monolith (to 10 mm) the O₂ remains undetected. However, a measurement was made at the 20 mm mark, 10 mm beyond the back face of the monolith, indicating the presence of 950 ppm O₂. The reemergence of O₂ downstream of the monolith is attributed to the same co-existence of active and inhibited states feature observed for the dry feed. As in the case of the persistence of multiplicity, the addition of H₂O to the feed does not impact the ability for inhibited and active conversion states to be sustained under the same conditions.

Conclusions

The combination of parametric evaluations of feed temperature and O₂ feed concentration on methane conversion and CO + CO₂ product distribution along with spatially-resolved measurements of species concentrations and temperature elucidates the steady-state behavior of the sub-stoichiometric (O₂/CH₄ < 2) methane oxidation on a Pt-Pd monolith catalyst.

The main finding of this study is the existence of steady state multiplicity that is not of a thermokinetic origin based on a rather low temperature rise. The rate multiplicity manifests as a clockwise hysteresis dependence of methane conversion on feed O₂ concentration. Spatial profiles for active channels reveals a two-zone behavior with methane oxidation being followed by methane steam reforming and water-gas shift. The spatial measurement reveal the co-existence of active and inhibited steady states in separate monolith channels. A second major finding is the novel co-existence of high and low conversion states based on measured concentration profiles. This unexpected phenomenon results in an intermediate methane conversion bounded by the more conventional uniform states. The two main findings suggest that any kinetic model must be intrinsically multi-valued and the corresponding reactor model must account for the nonuniform states. Modeling is underway to advance these concepts.

The addition of water to the feed serves to increase the methane conversion, underscoring the importance of methane steam reforming. The spatial profiles show concurrent oxidation and steam reforming, in contrast to the sequential behavior for dry feed. The multiplicity and nonuniform states persist with water addition. Future experiments concerning the effects of varied water and carbon dioxide concentration could help elucidate the behaviors of rich methane oxidation allowing for models to be developed to predict that behavior.

Acknowledgements

The authors gratefully acknowledge DOE Vehicle Technologies Office (project award number: DE-EE0008332) for funding. The supply of catalysts from CDTi (Oxnard, CA) is also acknowledged.

References

- [1] Z. Li, G.B. Hoflund, A Review on Complete Oxidation of Methane at Low Temperatures, *Journal of Natural Gas Chemistry*. 12 (2003) 153–160.
- [2] P. G elin, M. Primet, Complete oxidation of methane at low temperature over noble metal based catalysts: a review, *Appl Catal B*. 39 (2002) 1–37. [https://doi.org/10.1016/S0926-3373\(02\)00076-0](https://doi.org/10.1016/S0926-3373(02)00076-0).
- [3] S.H. Oh, P.J. Mitchell, R.M. Siewertt, Methane Oxidation over Alumina-Supported Noble Metal Catalysts with and without Cerium Additives, *J Catal*. 132 (1991) 287–301.
- [4] G.S. Bugosh, V.G. Easterling, I.A. Rusakova, M.P. Harold, Anomalous steady-state and spatio-temporal features of methane oxidation on Pt/Pd/Al₂O₃ monolith spanning lean and rich conditions, *Appl Catal B*. 165 (2015) 68–78. <https://doi.org/10.1016/j.apcatb.2014.09.058>.
- [5] Y.H. Chin, C. Buda, M. Neurock, E. Iglesia, Reactivity of chemisorbed oxygen atoms and their catalytic consequences during CH₄-O₂ catalysis on supported Pt clusters, *J Am Chem Soc*. 133 (2011) 15958–15978. <https://doi.org/10.1021/ja202411v>.
- [6] A. Hellman, A. Resta, N.M. Martin, J. Gustafson, A. Trincherro, P.A. Carlsson, O. Balmes, R. Felici, R. Van Rijn, J.W.M. Frenken, J.N. Andersen, E. Lundgren, H. Gr nbeck, The active phase of palladium during methane oxidation, *Journal of Physical Chemistry Letters*. 3 (2012) 678–682. <https://doi.org/10.1021/jz300069s>.
- [7] R. Abbasi, L. Wu, S.E. Wanke, R.E. Hayes, Kinetics of methane combustion over Pt and Pt-Pd catalysts, *Chemical Engineering Research and Design*. 90 (2012) 1930–1942. <https://doi.org/10.1016/j.cherd.2012.03.003>.
- [8] K. Persson, A. Ersson, K. Jansson, J.L.G. Fierro, S.G. J r s, Influence of molar ratio on Pd-Pt catalysts for methane combustion, *J Catal*. 243 (2006) 14–24. <https://doi.org/10.1016/j.jcat.2006.06.019>.

- [9] J. Park, D. Kim, S.W. Byun, H. Shin, Y. Ju, H. Min, Y.J. Kim, I. Heo, M.J. Hazlett, M. Kim, S.B. Kang, Impact of Pd:Pt ratio of Pd/Pt bimetallic catalyst on CH₄ oxidation, *Appl Catal B*. 316 (2022) 121623. <https://doi.org/10.1016/j.apcatb.2022.121623>.
- [10] R.H. Nibbelke, J.H.B.J. Hoebink, G.B. Marin, Kinetically induced multiplicity of steady states in integral catalytic reactors, *Chem Eng Sci*. 53 (1998) 2195–2210.
- [11] M.P. Harold, M.E. Garske, Kinetics and Multiple Rate States of CO Oxidation on Pt I. Model Development and Multiplicity Analysis, *J Catal*. 127 (1991) 524–552.
- [12] M.P. Harold, M.E. Garske, Kinetics and Multiple Rate States of CO Oxidation on Pt II. Linking UHV and Atmospheric Pressure Kinetic Behavior, *J Catal*. 127 (1991) 553–575.
- [13] M.P. Harold, D. Luss, AN EXPERIMENTAL STUDY OF STEADY-STATE MULTIPLICITY FEATURES OF TWO PARALLEL CATALYTIC REACTIONS, *Chem Eng Sci*. 40 (1985) 39–52.
- [14] M. P. Harold, M. Sheintuch, D. Luss, Analysis and Modeling of Multiplicity Features. 1. Nonisothermal Experiments, *Ind Eng Chem Res*. 26 (1987) 786–794.
- [15] M.P. Harold, M. Sheintuch, D. Luss, Analysis and Modeling of Multiplicity Features. 2. Isothermal Experiments, *Ind Eng Chem Res*. 26 (1987) 794–804.
- [16] R.M. Al Soubaihi, K.M. Saoud, J. Dutta, Critical review of low-temperature CO oxidation and hysteresis phenomenon on heterogeneous catalysts, *Catalysts*. 8 (2018). <https://doi.org/10.3390/catal8120660>.
- [17] A.N. Subbotin, B.S. Gudkov, Z.L. Dykh, V.L. Yakerson, N.D. Zelinsky, TEMPERATURE HYSTERESIS IN CO OXIDATION ON CATALYSTS OF VARIOUS NATURE, *Reaction Kinetics and Catalysis Letters*. 66 (n.d.) 97–104.
- [18] R. Raj, M.P. Harold, V. Balakotaiah, Steady-state and dynamic hysteresis effects during lean co-oxidation of CO and C₃H₆ over Pt/Al₂O₃ monolithic catalyst, *Chemical Engineering Journal*. 281 (2015) 322–333. <https://doi.org/10.1016/j.cej.2015.06.057>.
- [19] G. EIGENBERGER, KINETIC INSTABILITIES IN HETEROGENEOUSLY CATALYZED REACTIONS-I RATE MULTIPLICITY WITH LANGMUIR-TYPE KINETICS, *Chem Eng Sci*. 33 (1978) 1255–1261.
- [20] I.A. Chetyrin, A. V. Bukhtiyarov, I.P. Prosvirin, V.I. Bukhtiyarov, Investigation of concentration hysteresis in methane oxidation on bimetallic Pt–Pd/Al₂O₃ catalyst by in situ XPS and mass spectrometry, *Mendeleev Communications*. 31 (2021) 635–637. <https://doi.org/10.1016/j.mencom.2021.09.014>.
- [21] I.Y. Pakharukov, A.Y. Stakheev, I.E. Beck, Y. V. Zubavichus, V.Y. Murzin, V.N. Parmon, V.I. Bukhtiyarov, Concentration hysteresis in the oxidation of methane over Pt/γ-Al₂O₃: X-ray absorption spectroscopy and kinetic study, *ACS Catal*. 5 (2015) 2795–2804. <https://doi.org/10.1021/cs501964z>.

- [22] D. Dalle Nogare, S. Salemi, P. Biasi, P. Canu, Taking advantage of hysteresis in methane partial oxidation over Pt on honeycomb monolith, *Chem Eng Sci.* 66 (2011) 6341–6349. <https://doi.org/10.1016/j.ces.2011.04.029>.
- [23] A. Amin, A. Abedi, R. Hayes, M. Votsmeier, W. Epling, Methane oxidation hysteresis over Pt/Al₂O₃, *Appl Catal A Gen.* 478 (2014) 91–97. <https://doi.org/10.1016/j.apcata.2014.03.032>.
- [24] H. Nguyen, M.P. Harold, D. Luss, Spatiotemporal behavior of Pt/Rh/CeO₂/BaO catalyst during lean-rich cycling, *Chemical Engineering Journal.* 262 (2015) 464–477. <https://doi.org/10.1016/j.cej.2014.09.103>.
- [25] M. Hettel, C. Antinori, O. Deutschmann, CFD Evaluation of In Situ Probe Techniques for Catalytic Honeycomb Monoliths, *Emission Control Science and Technology.* 2 (2016) 188–203. <https://doi.org/10.1007/s40825-016-0043-1>.
- [26] H. Nguyen, P.Y. Peng, D. Luss, M.P. Harold, Assessing intrusion by the capillary during spatially resolved mass spectrometry measurement, *Chemical Engineering Journal.* 307 (2017) 845–859. <https://doi.org/10.1016/j.cej.2016.08.101>.
- [27] J. Sá, D.L.A. Fernandes, F. Aiouache, A. Goguet, C. Hardacre, D. Lundie, W. Naeem, W.P. Partridge, C. Stere, SpaciMS: Spatial and temporal operando resolution of reactions within catalytic monoliths, *Analyst.* 135 (2010) 2260–2272. <https://doi.org/10.1039/c0an00303d>.
- [28] P.Y. Peng, H. Nguyen, M.P. Harold, D. Luss, Spatio-Temporal Phenomena in Monolithic Reactors Measured by Combined Spatially-Resolved Mass Spectrometry and Optical Frequency Domain Reflectometry, in: *Advances in Chemical Engineering*, 2017. <https://doi.org/10.1016/bs.ache.2017.07.001>.
- [29] H. Nguyen, M.P. Harold, D. Luss, Optical frequency domain reflectometry measurements of spatio-temporal temperature inside catalytic reactors: Applied to study wrong-way behavior, *Chemical Engineering Journal.* 234 (2013) 312–317. <https://doi.org/10.1016/j.cej.2013.08.074>.
- [30] B.J. Soller, D.K. Gifford, M.S. Wolfe, M.E. Froggatt, High resolution optical frequency domain reflectometry for characterization of components and assemblies, *Opt Express.* 13 (2005) 666. <https://doi.org/10.1364/opex.13.000666>.
- [31] C. Coney, C. Stere, P. Millington, A. Raj, S. Wilkinson, M. Caracotsios, G. McCullough, C. Hardacre, K. Morgan, D. Thompsett, A. Goguet, Spatially-resolved investigation of the water inhibition of methane oxidation over palladium, *Catal Sci Technol.* 10 (2020) 1858–1874. <https://doi.org/10.1039/d0cy00154f>.
- [32] O. Korup, C.F. Goldsmith, G. Weinberg, M. Geske, T. Kandemir, R. Schlögl, R. Horn, Catalytic partial oxidation of methane on platinum investigated by spatial reactor profiles, spatially resolved spectroscopy, and microkinetic modeling, *J Catal.* 297 (2013) 1–16. <https://doi.org/10.1016/j.jcat.2012.08.022>.
- [33] B. Li, S. Kado, Y. Mukainakano, M. Nurunnabi, T. Miyao, S. Naito, K. Kunimori, K. Tomishige, Temperature profile of catalyst bed during oxidative steam reforming of methane

over Pt-Ni bimetallic catalysts, *Appl Catal A Gen.* 304 (2006) 62–71.
<https://doi.org/10.1016/J.APCATA.2006.02.025>.

- [34] N.Z. Muradov, T.N. Veziroğlu, From hydrocarbon to hydrogen-carbon to hydrogen economy, *Int J Hydrogen Energy.* 30 (2005) 225–237. <https://doi.org/10.1016/j.ijhydene.2004.03.033>.

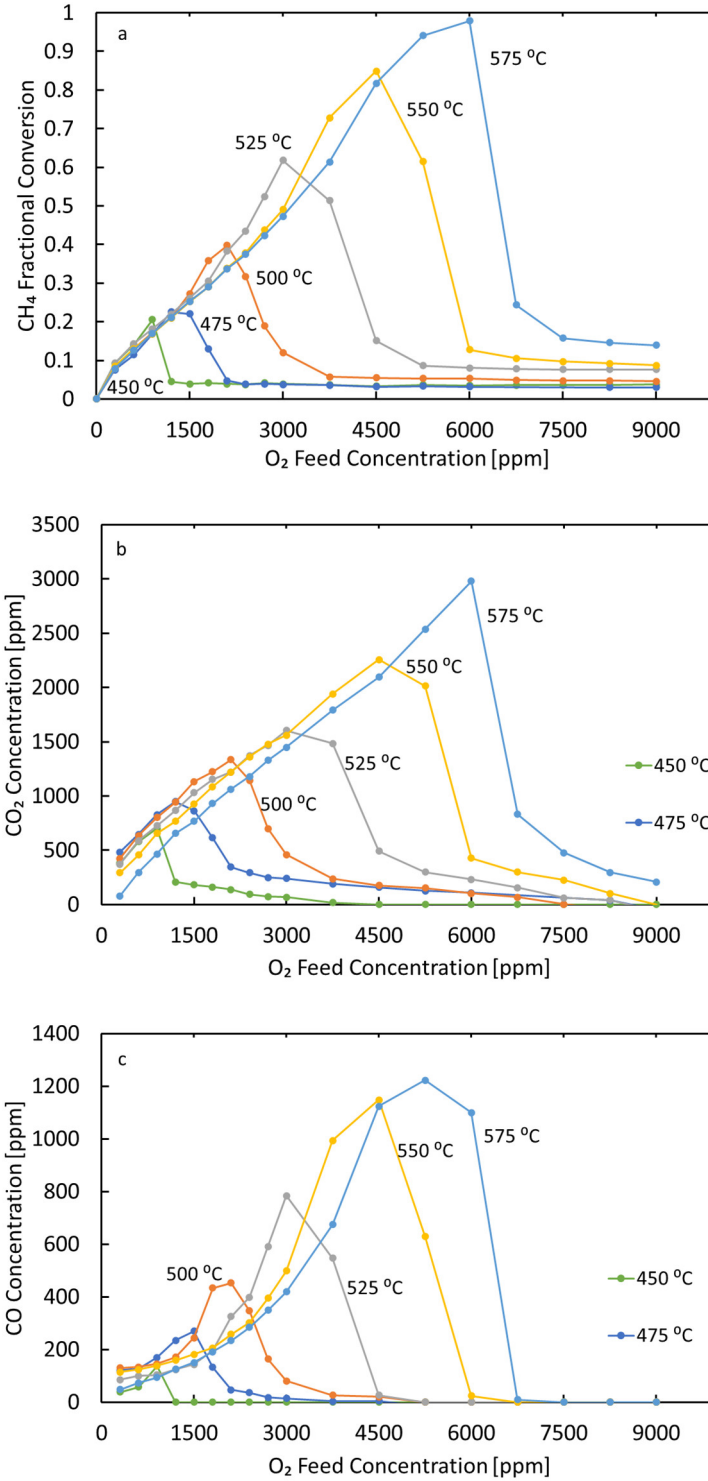


Figure 1. (a) Inlet temperature and O₂ feed concentration impact on CH₄ conversion; (b) Feed temperature and O₂ feed concentration impact on CO₂ effluent concentration; (c) The impact of feed temperature and O₂ feed concentration on CO effluent concentration.

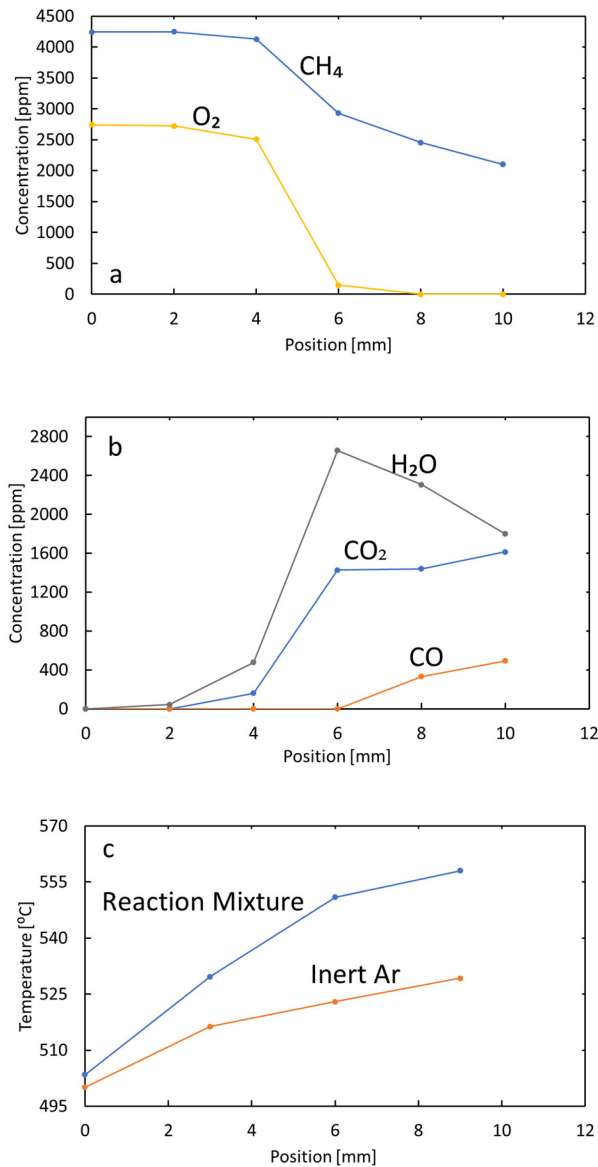


Figure 2. (a) Spatial concentration profiles for CH_4 and O_2 for 525 $^{\circ}\text{C}$ and 2700 ppm O_2 feed concentration; (b) Spatial concentration profiles of CO and CO_2 and calculated H_2O for 525 $^{\circ}\text{C}$ and 2700 ppm O_2 feed concentration; (c) Spatial temperature for 2700 ppm O_2 feed concentration and 525 $^{\circ}\text{C}$.

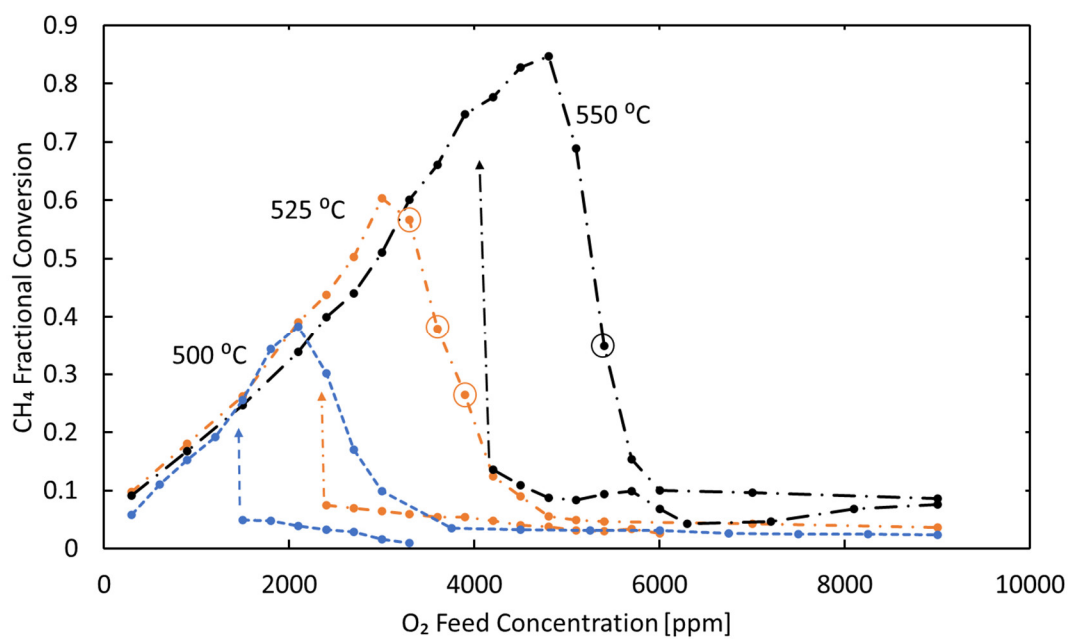


Figure 3. Clockwise hysteresis loops of methane oxidation versus O₂ feed concentration at feed temperatures of 500, 525, and 550 °C. Circled points are those for which nonuniform states were observed.

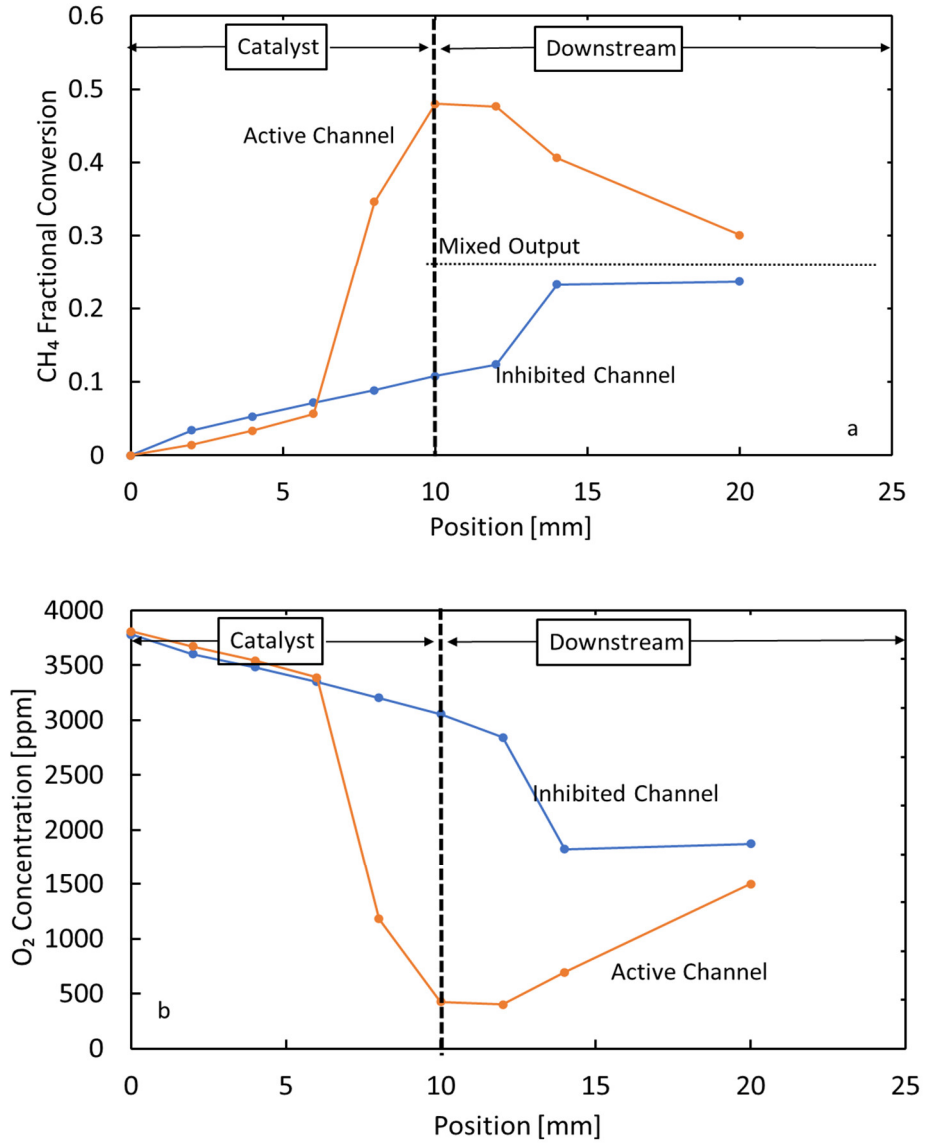


Figure 4. (a) Spatial profiles for methane conversion for 525 °C and 3900 feed O₂ showing two different steady states; (b) Spatial profiles for O₂ for 525 °C and 3900 feed O₂ showing two different steady states.

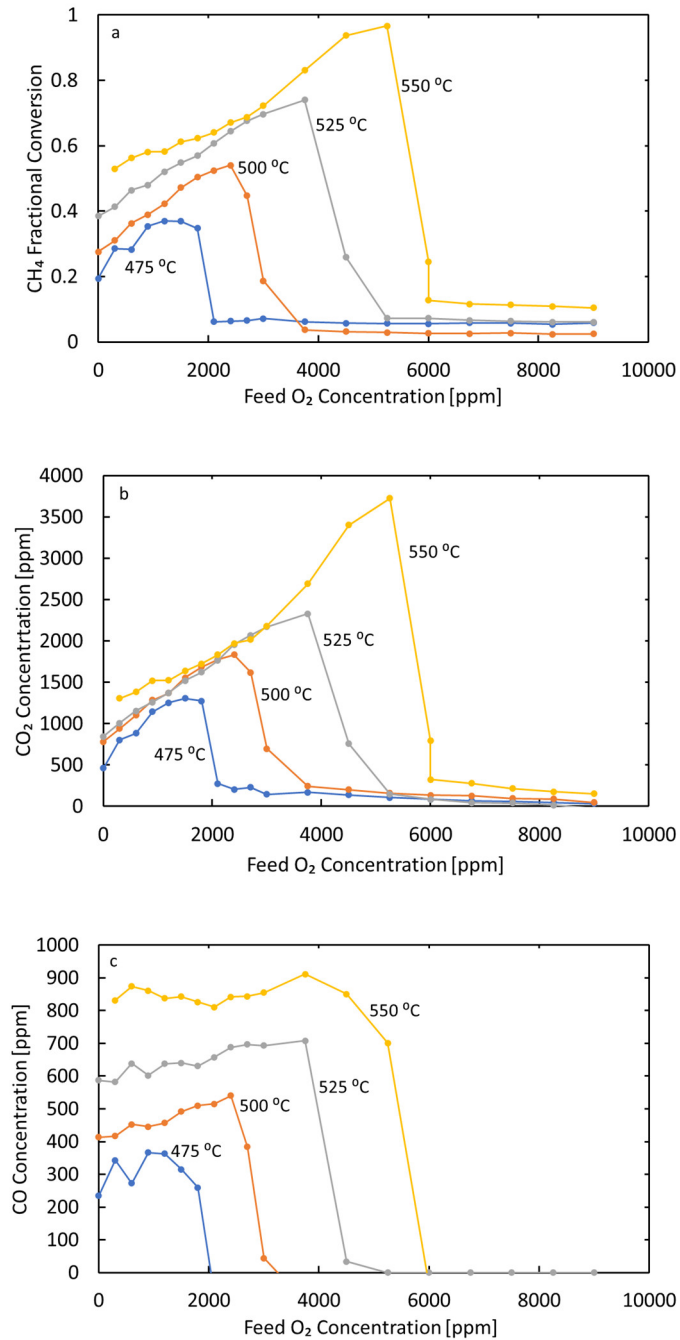


Figure 5. (a) Impact of inlet temperature and O₂ concentration on methane conversion with 2.5% H₂O in the feed; (b) Impact of inlet temperature and O₂ concentration on CO₂ concentration with 2.5% H₂O in the feed; (c) Impact of inlet temperature and O₂ concentration on CO concentration with 2.5% H₂O in the feed.

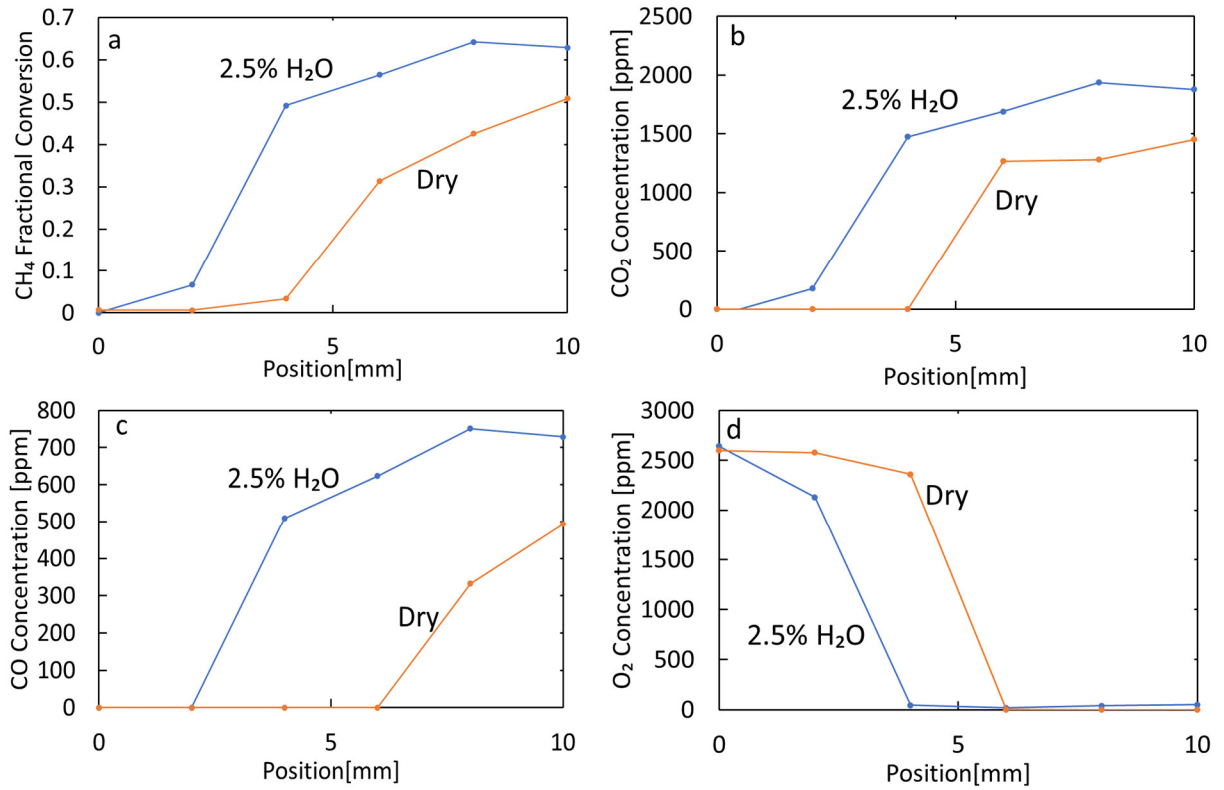


Figure 6. (a) Spatial CH₄ conversion profile for 2700 ppm O₂ and 525 °C for 2.5% H₂O vs. dry; (b) Spatial CO₂ concentration profile for 2700 ppm O₂ and 525 °C for 2.5% H₂O vs. dry; (c) Spatial CO concentration profile for 2700 ppm O₂ and 525 °C for 2.5% H₂O vs. dry; (d) Spatial O₂ concentration profile for 2700 ppm O₂ and 525 °C for 2.5% H₂O vs. dry.

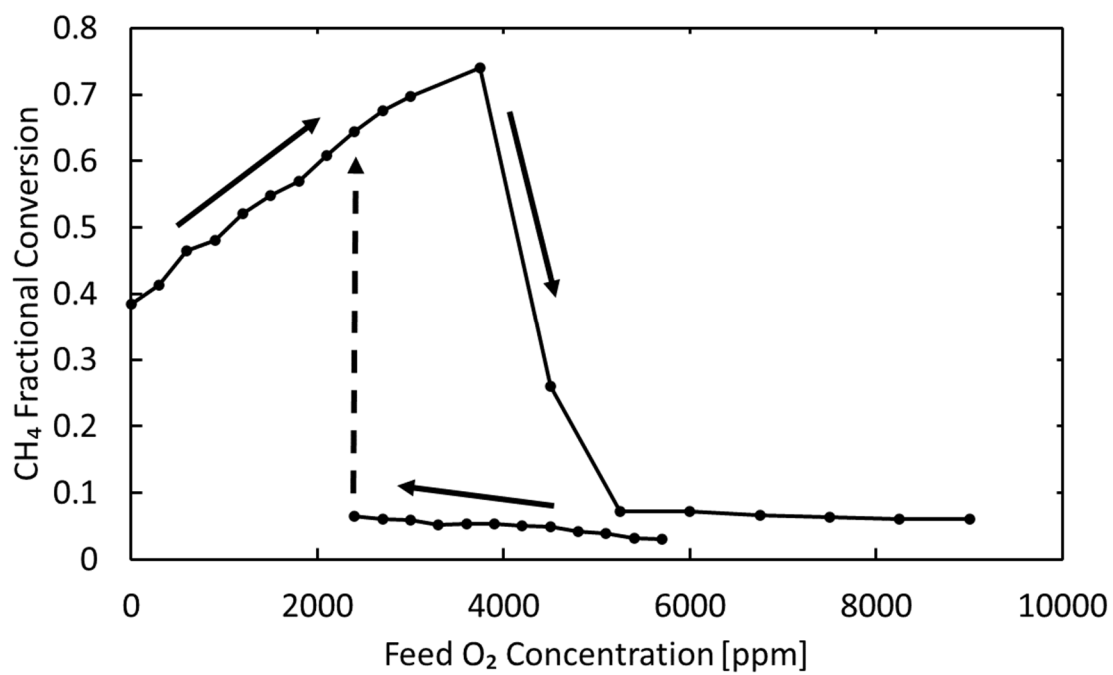


Figure 7. Clockwise hysteresis loop for methane oxidation at 525 °C with 2.5% H₂O in the feed.

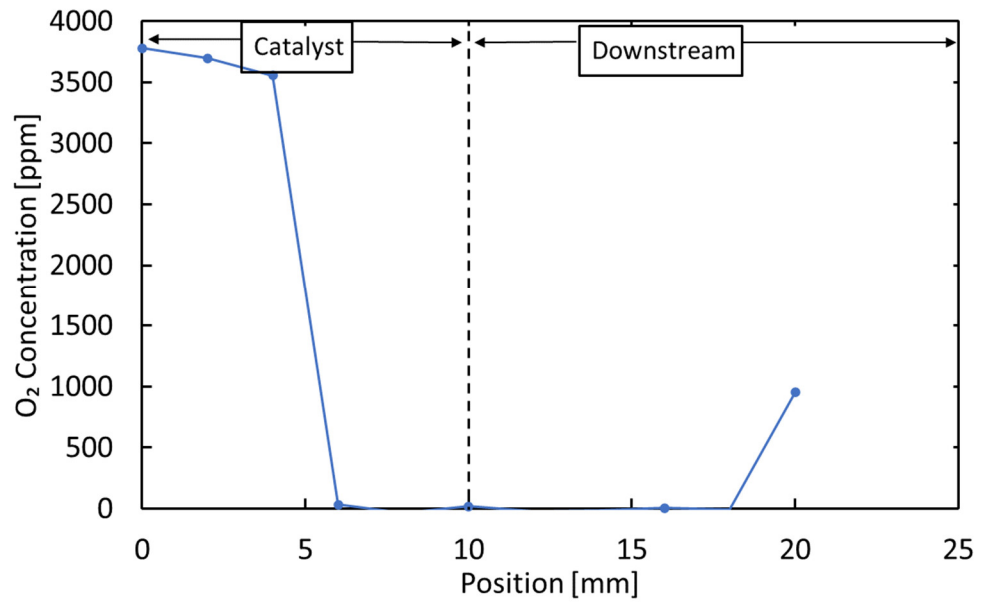


Figure 8. Spatial concentration profile of O₂ for 525 °C and 3900 ppm inlet O₂.

Rich Methane Oxidation on Pt/Pd/Al₂O₃: Steady State Performance, Multiplicity Features, and Spatial Patterns

Jonathan Ratcliff, Kyle Karinshak, and Michael P. Harold*

William A. Brookshire Department of Chemical and Biomolecular Engineering, University of Houston, Houston, Texas 77204, USA

*Corresponding author: mpharold@central.uh.edu

Supplementary Material

S.1 Explanation of CO and CO₂ Behaviors for Dry Oxidation

Complete O₂ conversion is established in the *active regime* to the left of the CH₄ conversion maximum. The *active regime* is clearly limited by oxygen given the near independence of feed temperature. Knowing this fact, the above-described dependencies of the CH₄ conversion and CO₂:CO selectivity on the feed temperature are largely a result of differences in O₂ utilization by complete and partial oxidation. This is illustrated by calculating the methane conversion along the active branch assuming complete conversion of O₂ for two cases; one for both complete oxidation and the other for partial oxidation. The complete oxidation locus bounds the conversion data from below while the partial oxidation locus bounds the data from above. This reaffirms that changes in the CH₄ conversion and CO₂ and CO effluent concentrations with feed temperature for a fixed O₂ feed concentration is a result of shifting extents of complete and partial oxidation. For example, at 3000 ppm O₂, the CH₄ conversion decreases from 65% at 525 °C to 50% at 575 °C. In the same experiments the CO concentration decreases from 800 ppm to 425 ppm while the CO₂ concentration only slightly decreases from ~1600 to ~1450 ppm. Thus, an increase in feed temperature expands the extent of complete oxidation within the monolith. A contributing factor

is increased downstream consumption of CO by its reaction with generated H₂O; i.e., WGS. We return to this point later.

The larger extent of partial oxidation near the inhibition point is evident in the convex shape of the CO concentration data (Fig. 1c). At O₂ feed concentrations below ~1500 ppm the CO curves at different feed temperatures are nearly flat. As the O₂ feed concentration is increased for a fixed feed temperature, the CO produced increases nonlinearly while the CO₂ produced only increases linearly. The unusual shape of the CO curves warrants some consideration. The flat section in the CO concentration at lower O₂ feed concentration likely originates from the lack of water in the dry feed. In other words, any water that is needed for steam reforming (R4) or water-gas shift (R3) must be generated by upstream total oxidation. Therefore, at a low CH₄ conversion the H₂O concentration is also low, limiting the extents of both SMR and WGS. Further, if any steam reforming does occur, the CO formed is likely to be consumed by WGS, as was seen in the spatial profiles (Fig. 2b). As the O₂ feed concentration increases and therefore the amount of H₂O produced does as well, the extent of downstream SMR increases. This results in a disproportionate increase in CO generated compared to O₂ added, causing the CO profile to have the convex shape. This trend is exacerbated by the partial oxidation reaction selectivity; i.e., as partial oxidation becomes relatively more significant, a larger amount of CO is formed resulting in a more pronounced convex shape.

The partial oxidation selectivity is driven by two parameters, the O₂ feed concentration and feed temperature. A higher O₂ concentration and/or lower feed temperature will extend the length of the aerobic zone within the monolith channel. In the front part of the zone the oxidation is inhibited and the O₂ profile is rather flat. Further downstream the inhibition lessens as O₂ is consumed via complete oxidation. The O₂ consumption leads to a steeper decline in the local

O₂/CH₄ ratio. The spatial profiles for the 525 °C, 2700 ppm O₂ experiment in Fig. 2a show the inhibited, complete oxidation zone between 0 and 4 mm and the partial oxidation zone between 4 and 6 mm. The dearth of O₂ undoubtedly increases the contribution of partial oxidation.

S.2 Extent of Reaction Calculations

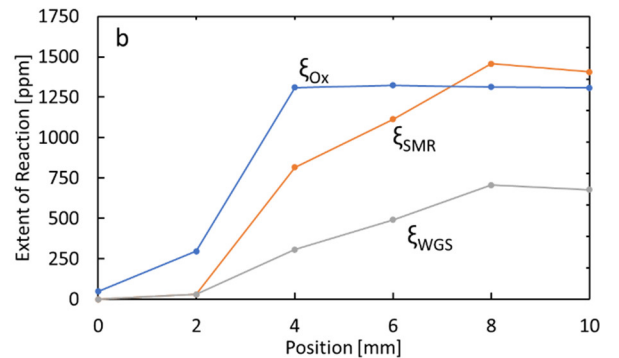
To determine the extent of reactions, first a set of reactions needed to be decided upon. Since there are six total species and three elements composing those species, a system of three reactions completely describes the system. The reactions chosen to describe the system are total oxidation, steam reforming, and water-gas shift. Calculation of the extent of reaction is done via using the concentrations of species at each spatial point for a given inlet condition. The system of equations used to determine the extent of reaction is as follows:

$$\xi_{Ox,x} = \frac{O_{2,in} - O_{2,x}}{2} \quad (S1)$$

$$\xi_{SMR,x} = CH_{4,in} - \xi_{Ox,x} - CH_{4,x} \quad (S2)$$

$$\xi_{WGS,x} = \xi_{SMR,x} - CO_x \quad (S3)$$

The subscript x denotes the values at the current position within the catalyst. The concentrations and extent of reactions are in parts per million.



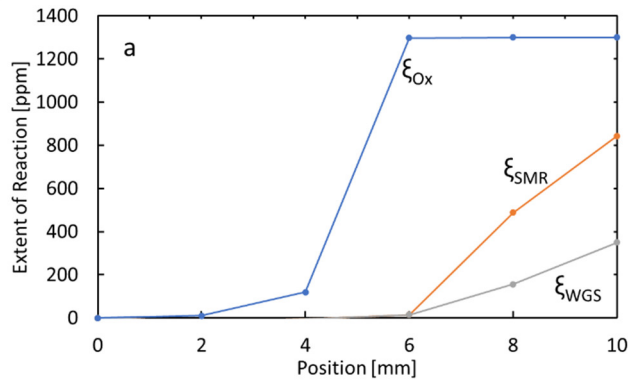
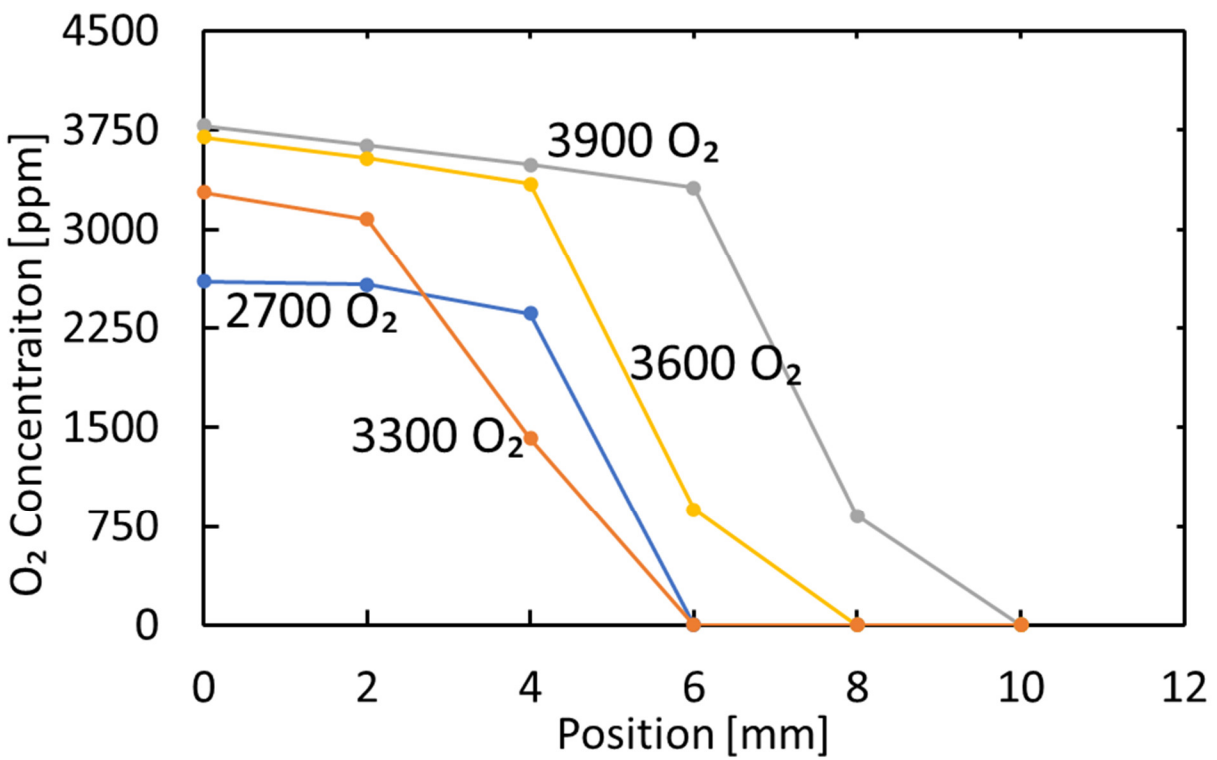
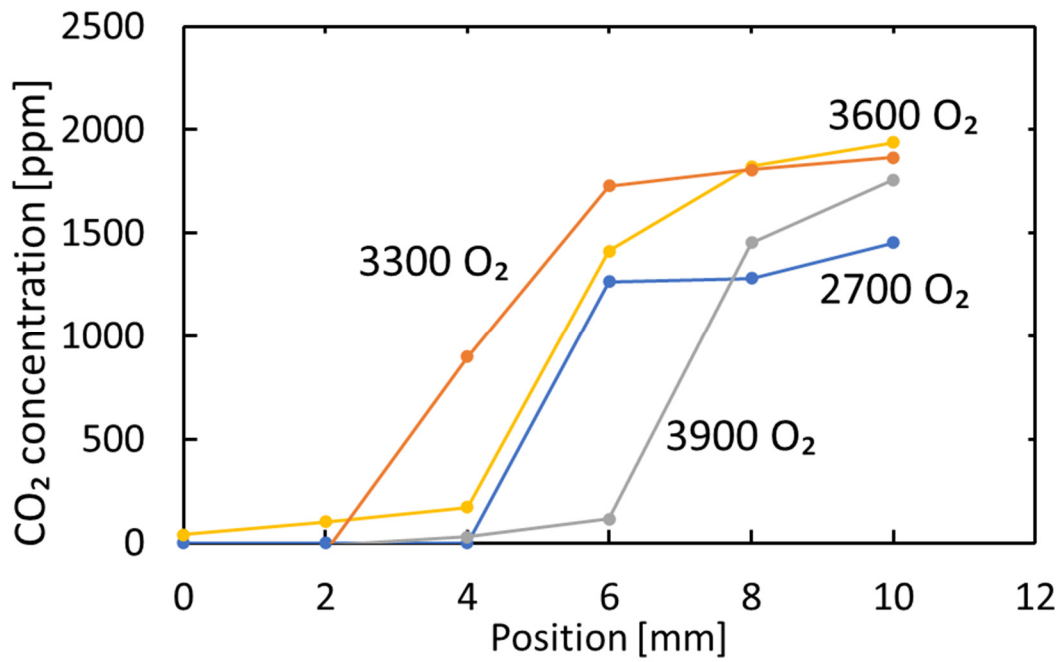
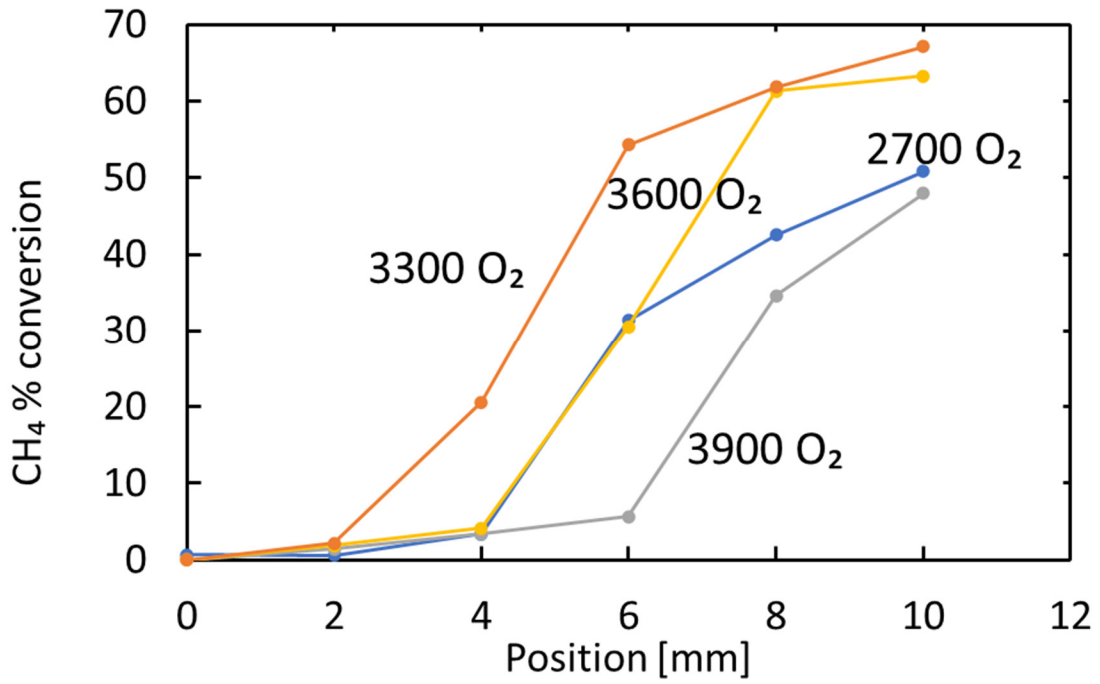


Figure S.1 a) Extent of reactions for 2700 O_2 , 525 °C under dry conditions b) Extent of reactions for 2700 O_2 , 525 °C, 2.5% H_2O

S.3 Shifting O_2 depletion zone





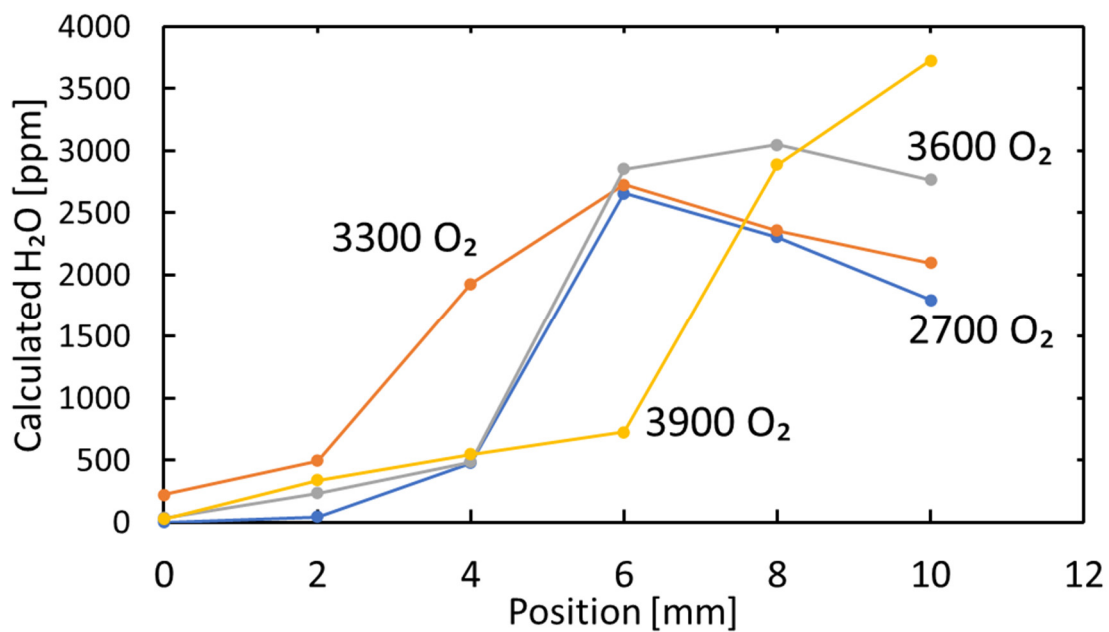
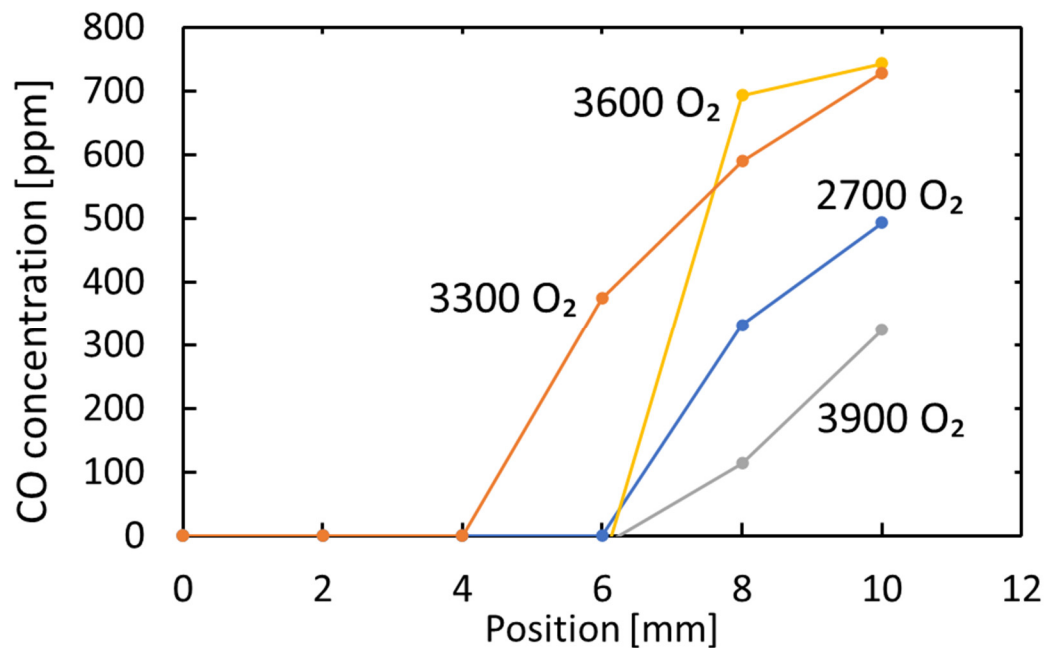


Figure S.2: A) Spatial O₂ profiles for varied inlet O₂ concentrations at 525 °C (2700, 3300, 3600, 3900) B) Spatial CH₄ conversion profiles for varied inlet O₂ concentrations at 525 °C (2700, 3300, 3600, 3900) C) CO₂ profiles D) CO profiles E) Calculated H₂O profiles

Despite the concentration of H₂O not being measured during experiments, it can be calculated using the oxygen balance. The species that contain oxygen are H₂O, CO, CO₂, and O₂. By measuring CO, CO₂, and O₂ any imbalance that occurs in the oxygen balance is from the formation of non-measured H₂O so by determining balance at any given position, a rough estimate of H₂O is obtained. This is not an exact value since there are inherent inaccuracies that can arise using an atom balance to determine a species concentration but provides a good estimate.

S.4 Adiabatic temperature rise estimate

Using the ratio of CO to CO₂ can be used to provide a rough estimate for what the adiabatic temperature rise should be. To do this, the first assumption made is that the only reactions occurring are partial and total oxidation. Total oxidation is responsible for CO₂ production and partial oxidation for CO production. So the ratio of CO to CO₂ is equivalent to the ratio of total oxidation to partial oxidation. This can be used to determine the extent of partial oxidation in terms of total oxidation as follows:

$$\frac{CO}{CO_2} = \frac{\xi_{POx}}{\xi_{TOx}} \quad \xi_{POx} = \frac{CO}{CO_2} \xi_{TOx} \quad (S4)$$

Then the value of ξ_{POx} is used in the oxygen species balance. Since this is only used for active channels where all the O₂ is consumed, the balance simplifies to:

$$2\xi_{TOx} + 1/2 \left(\frac{CO}{CO_2} \xi_{POx} \right) = C_{O_2,in} \quad (S5)$$

This is then used to solve for the extents of both total oxidation and partial oxidation resulting in:

$$\xi_{TOx} = \frac{C_{O_2,in}}{2 + \frac{CO}{2CO_2}} \quad \xi_{POx} = \frac{\left(\frac{CO}{CO_2}\right)C_{O_2,in}}{2 + \frac{CO}{2CO_2}} \quad (S6)$$

Those extents of reaction are then both used in the adiabatic temperature rise equation as follows:

$$\Delta T_{ad} = \frac{\Delta H_{TOx} \xi_{TOx}}{\langle c_p \rangle} + \frac{\Delta H_{POx} \xi_{POx}}{\langle c_p \rangle} \quad (S7)$$

This equation produces the maximum possible temperature rise for an adiabatic system with a composition of CO and CO₂ as seen. Using a value of 2700 ppm O₂ as an inlet condition to test, the calculated temperature rise is 46 °C in comparison to the value of 29 °C seen under experimental conditions. The reason for the difference can be attributed to two key factors. The first of which is this system only using exothermic reactions to calculate the rise, thereby eliminating endothermic reforming reactions and their impact on catalyst temperature. Also, the other key factor is this system is not truly adiabatic, meaning a non-zero amount of this heat is lost to the surroundings.

S.5 Carbon balance for O₂ sweeps under dry conditions

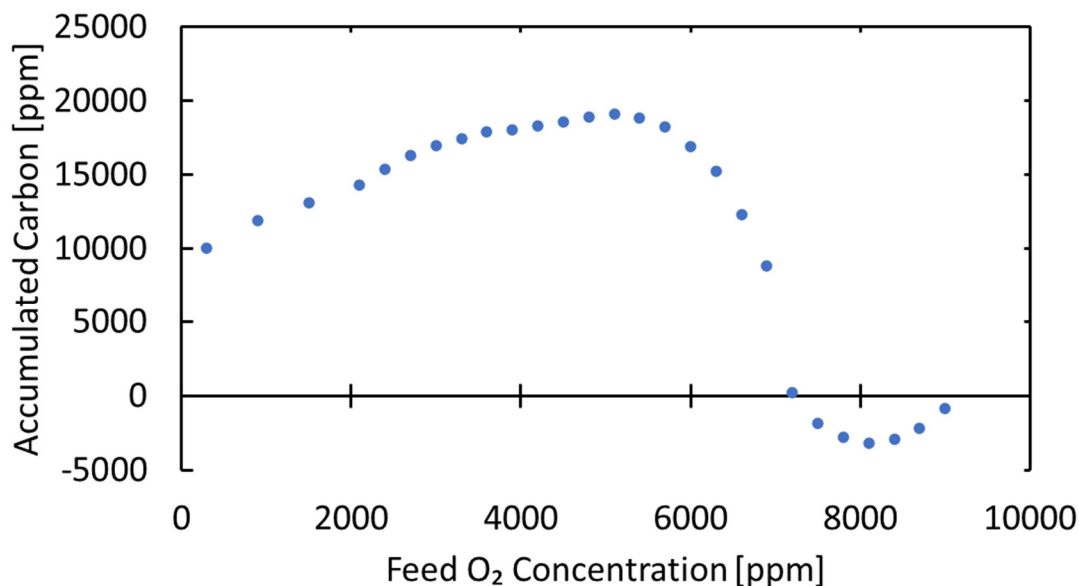


Figure S.3: Accumulated carbon as the inlet O₂ concentration is varied for 575 °C

Figure S.3 was calculated by determining the carbon balance for the individual inlet O₂ concentrations, where positive values indicate more carbon entering the catalyst than leaving. This value was then multiplied by the time spent at that point to gain an idea of the accumulation occurring. A gradual accumulation of carbon is observed as the experiment progresses, as inlet O₂ concentrations were varied from low to high. The reason the 300 ppm point shows large initial accumulation is that this point is held for longest of any of the tested points in order to ensure steady state. As the concentration of O₂ gets large enough, the accumulation starts to decrease suggesting that the oxygen is removing surface carbon. Eventually as the concentration of inlet O₂ approaches that of stoichiometry for total oxidation, the accumulation approaches zero meaning the surface carbon that formed has now been largely removed.

This issue of accumulating carbon followed by a corresponding burn-off as the O₂ concentrations increase was only seen for the 575 °C case. Lower temperatures and the data where water is included do not show this behavior of accumulating carbon and removing it later in the

experiment. The trends will remain relatively constant in regions of high activity and then be prone to drifting, often showing “accumulation” despite being in an inhibited high O₂ state, due to errors with low concentration detection of CO₂ by the mass spectrometer. This is because when the concentration of CO₂ is low, the current is more prone to noise reducing the accuracy in these sections. The accuracy of CH₄ and O₂ in these sections remains strong since the concentrations are high producing a constant signal.

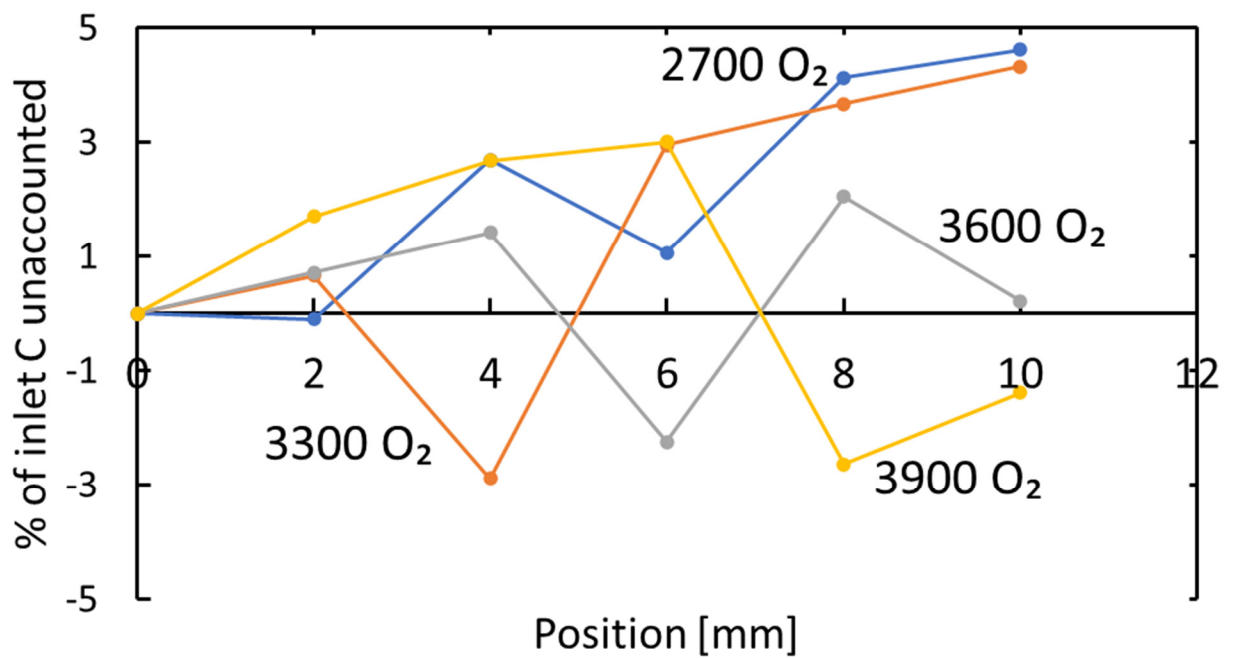


Figure S.4: Carbon balance for spatial profiles of 2700, 3300, 3600, 3900 O₂ for 525 °C

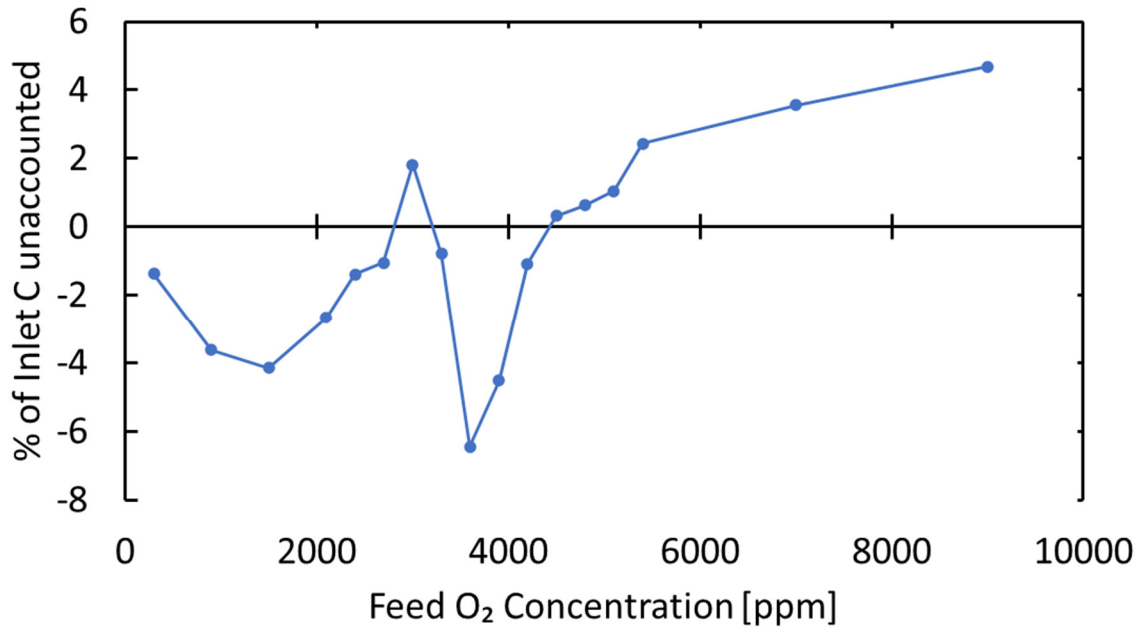


Figure S.5: Carbon balance for bulk effluent of O₂ sweep for 525 °C

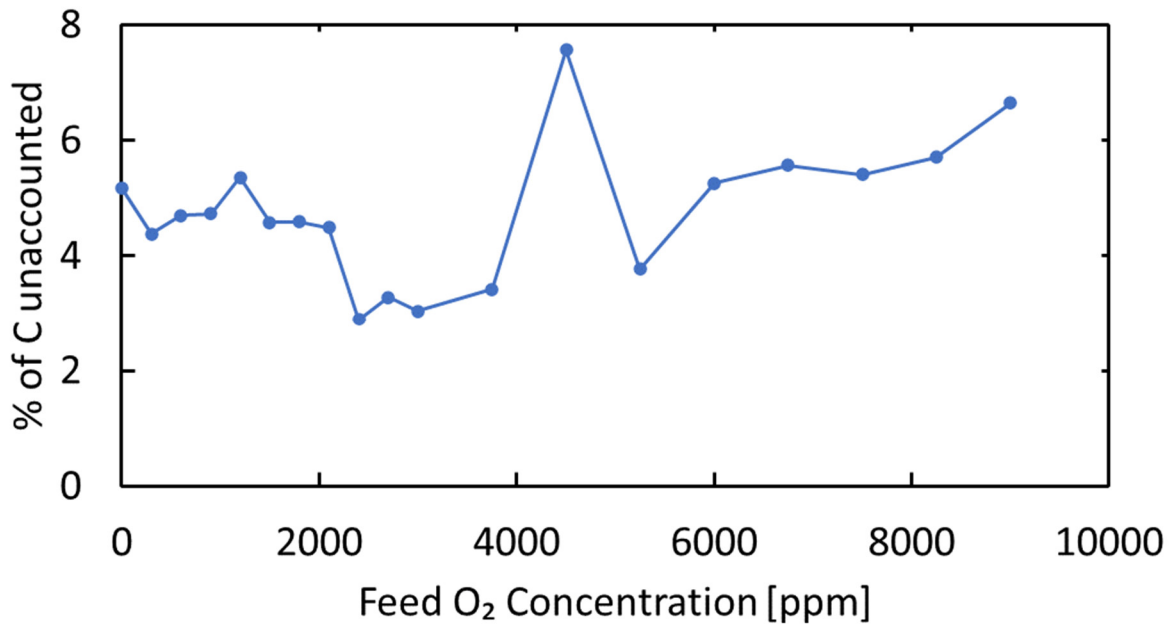


Figure S.6: Carbon balance for 2.5% H₂O and 525 °C

